Biomech Model Mechanobiol (2013) 12:685–703
DOI 10.1007/s10237-012-0434-3

ORIGINAL PAPER

An experimental and computational investigation of the post-yield behaviour of trabecular bone during vertebral device subsidence

Nicola Kelly · Noel M. Harrison · Pat McDonnell · J. Patrick McGarry

Received: 8 June 2012 / Accepted: 18 August 2012 / Published online: 16 September 2012

Abstract Interbody fusion device subsidence has been reported clinically. An enhanced understanding of the mechanical behaviour of the surrounding bone would allow for accurate predictions of vertebral subsidence. The multiaxial inelastic behaviour of trabecular bone is investigated at a microscale and macroscale level. The post-yield behaviour of trabecular bone under hydrostatic and confined compression is investigated using microcomputed tomography-derived microstructural models, elucidating a mechanism of pressure-dependent yielding at the macroscopic level. Specifically, microstructural trabecular simulations predict a distinctive yield point in the apparent stress–strain curve under uniaxial, confined and hydrostatic compression. Such distinctive apparent stress–strain behaviour results from localised stress concentrations and material yielding in the trabecular microstructure. This phenomenon is shown to be independent of the plasticity formulation employed at a trabecular level. The distinctive response can be accurately captured by a continuum model using a crushable foam plasticity formulation in which pressure-dependent yielding occurs. Vertebral device subsidence experiments are also performed, providing measurements of the trabecular plastic zone. It is demonstrated that a pressure-dependent plasticity formulation must be used for continuum level macroscale models of trabecular bone in order to replicate the experimental observations, further supporting the microscale investigations. Using a crushable foam plasticity formulation in the simulation of vertebral subsidence, it is shown that the predicted subsidence force and plastic zone size correspond closely with the experimental measurements. In contrast, the use of von Mises, Drucker–Prager and Hill plasticity formulations for continuum trabecular bone models lead to over prediction of the subsidence force and plastic zone.

Keywords Trabecular bone · Pressure-dependent yielding · Hydrostatic compression · Confined compression · microCT finite element analysis · Vertebral subsidence · Crushable foam

N. Kelly · N. M. Harrison · P. McDonnell · J. P. McGarry (✉)
Department of Mechanical and Biomedical Engineering,
National University of Ireland, Galway, Ireland
e-mail: patrick.mcgarry@nuigalway.ie

N. Kelly · N. M. Harrison · P. McDonnell · J. P. McGarry
National Centre for Biomedical Engineering Science,
National University of Ireland, Galway, Ireland

1 Introduction

Low back pain is a major health care problem, and an interbody fusion device (IFD) endeavours to replace a damaged or diseased intervertebral disc. IFDs often contain bone graft material to promote rigid fixation of the adjacent vertebrae. The metallic IFDs are significantly stiffer than the natural intervertebral disc and do not mimic the natural disc geometry. A range of IFD subsidence rates (3–76.7 %) have been reported clinically (Beutler and Peppelman 2003; Choi and Sung 2006; Chen et al. 2005). The vertebral endplates, the superior and inferior surfaces of the vertebral body, are composed of cortical bone. Various IFD designs require different bony endplate preparation techniques: intact; partial removal; complete removal. Removal of the stiffer cortical endplate exposes a host bed of bleeding trabecular bone (potentially osteogenic cells), which is advantageous from a biological point of view allowing bone fusion with the graft material. A number of in vitro investigations into the effect of endplate removal on the vertebral subsidence force have provided conflicting recommendations including endplate preservation (Lim et al. 2001; Oxland et al. 2003); partial

endplate removal (Steffen et al. 2000; Lowe et al. 2004); and complete endplate removal (Hollowell et al. 1996; Closkey et al. 1993). Regardless of the endplate preparation technique, the insertion of a stiff metallic IFD will induce significant stress concentrations in the surrounding bone. An enhanced understanding of the mechanical behaviour of the surrounding bone would allow for accurate predictions of vertebral subsidence, ultimately leading to improved IFD design and a reduced risk of subsidence.

The present study investigates vertebral device subsidence into the underlying trabecular bone that entails finite deformation and inelastic material behaviour. A complex stress state occurs due to the natural confinement of trabecular bone by a stiff cortical shell leading to significant pressure stress and large inelastic deformation. This suggests that it is essential to correctly model the multiaxial yield behaviour of trabecular bone to accurately predict subsidence. The importance of using an appropriate continuum constitutive plasticity formulation for an accurate prediction of the macroscale plastic deformation of trabecular bone during vertebral subsidence is, therefore, investigated.

To characterise the mechanical properties of trabecular bone, previous studies have primarily relied on uniaxial compression testing of representative samples of trabecular bone (Goldstein 1987; Røhl et al. 1991; Kopperdahl and Keaveny 1998; Morgan and Keaveny 2001; Keaveny et al. 1993; Keyak et al. 1996). Few studies have performed confined compression testing (Kelly and McGarry 2012; Linde and Hvid 1989; Charlebois et al. 2010b) or multiaxial compression testing (Fenech and Keaveny 1999; Keaveny et al. 1999; Rincon-Kohli and Zysset 2009) although trabecular bone is naturally constrained in vivo by the surrounding cortex. Complex loading configurations such as hydrostatic and confined compression, which involve the development of high trabecular pressures, should be considered to elucidate the multiaxial yield behaviour of trabecular bone. Recently published experiments demonstrate that confined compression (Charlebois et al. 2010b; Kelly and McGarry 2012) and multiaxial compression (Rincon-Kohli and Zysset 2009) loading of trabecular bone lead to apparent stress–strain curves that exhibit a distinctive yield point. Further, Kelly and McGarry (2012) demonstrated that simulation of this apparent response to confined compression using a continuum model requires the use of a pressure-dependent yield formulation (i.e., a formulation in which a purely hydrostatic stress state can result in material yielding, unlike the conventional pressure-independent von Mises (VM) plasticity formulation).

In addition to the macroscale investigation of vertebral subsidence, a microstructural analysis of trabecular bone plasticity is also performed. Microcomputed tomography (μCT)-based finite element (FE) models provide an accurate representation of the trabecular microarchitecture, however, due to high computational expense they are usually limited in terms of contact conditions, material behaviour and deformation. The use of microstructural models of representative trabecular bone samples to elucidate the inelastic behaviour can lead to the development of accurate continuum models, as demonstrated in the present study which may be used for macroscale applications with complex boundary and contact conditions, finite deformation and non-linear material behaviour.

Using microstructural voxel-based trabecular geometry with linear elastic material models, several studies have simulated the response of representative samples of trabecular bone to uniaxial compression (Harrison et al. 2008; Nagaraja et al. 2005; Müller and Rüegsegger 1995; Van Rietbergen et al. 1995). A number of studies have simulated non-linear trabecular behaviour by reducing the elastic modulus of the trabecular material when the principal strain at a material point exceeds a predefined value (Bayraktar et al. 2004; Bayraktar and Keaveny 2004; Niebur et al. 2000, 2002; Guillén et al. 2011; Verhulp et al. 2008). Verhulp et al. (2008) simulated uniaxial compression using μCT-based trabecular geometry with a perfectly-plastic VM plasticity formulation, while Harrison et al. (2012) simulated material damage and fracture in the trabecular microarchitecture, also under uniaxial compression. Apart from the studies of Niebur et al. (2002) and Bayraktar et al. (2004), in which biaxial (triaxial stress) and axial-shear testing was simulated using the principal strain-based modulus reduction model, none of these μCT studies has investigated the role of microstructural architecture in the multiaxial yielding of trabecular bone at the apparent level by considering loading configurations other than uniaxial compression. Van Rietbergen et al. (1995) and Boyd et al. (2002) considered confined compression of microstructural trabecular specimens, which were restricted to the elastic regime with maximum apparent strains of 1 %, again assuming linear elastic material behaviour.

The present study provides a link between the microscale (trabeculae) and macroscale inelastic behaviour of trabecular bone. The first objective of the study is to implement uniaxial, hydrostatic and confined compression for microstructural-based models of a representative sample of the trabecular bone microstructure in order to predict the multiaxial apparent yield behaviour. Specifically, the following issue is investigated: if a pressure-independent plasticity formulation is used to represent the material behaviour of individual trabeculae in a μCT model, will the predicted apparent stress–strain curves for hydrostatic and confined compression exhibit distinctive yielding? The second objective is to investigate the importance of using an appropriate continuum constitutive plasticity formulation for an accurate prediction of the macroscale plastic deformation of trabecular bone in order to accurately simulate the experimental subsidence of a vertebral IFD.

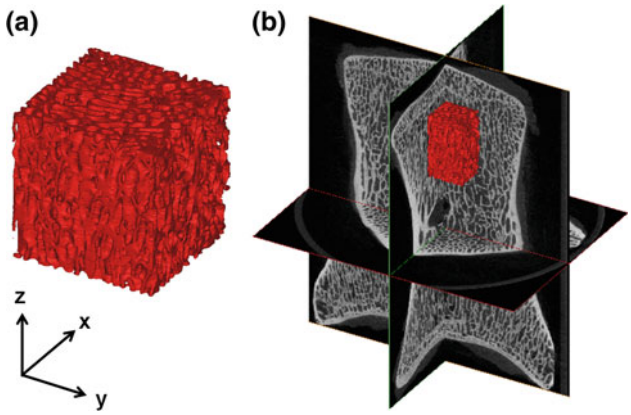

Fig. 1 **a** 8 mm trabecular bone μCT-based cube model. The z-direction is the superior-inferior (on-axis) loading direction, **b** L6 vertebra with the 8 mm cube of trabecular bone taken from the superior region of the vertebra

2 Materials and methods

2.1 Computational modelling of a representative trabecular bone sample

In order to investigate the roles of trabecular bone microstructure on apparent yielding, 3D 8 mm cube FE models of the trabecular bone microstructure were created from a lumbar ovine vertebra obtained from the PRTLI 'Bone for Life' project (Prendergast and McHugh 2004) using μCT images at 72 μm resolution (μCT 40, Scanco Medical AG, Basserdorf, Switzerland) consisting of approximately 270,000 four-noded tetrahedral elements (v14.11 Mimics and v6.0 3matic, Materialise, Leuven, Belgium) (Fig. 1). An elastic perfectly-plastic VM plasticity formulation was implemented, which does not include any pressure-dependent yielding in the trabecular material. Three different simulations were performed: uniaxial compression; hydrostatic compression; and confined compression. The tests were simulated in the superior-inferior direction where the specimens were oriented parallel to the axis of loading (on-axis). Apparent stress–strain curves were created for each loading configuration. The simulations investigated whether apparent yielding of trabecular bone (as demonstrated by Kelly and McGarry 2012) can be captured using a simple VM plasticity formulation in addition to an explicit representation of the trabecular bone microarchitecture. Simulations were also performed in which the Drucker–Prager (DP) plasticity formulation was used to model the trabecular material. Based on nanoindentation results from individual ovine vertebral trabeculae (Harrison et al. 2008), a local trabecular tissue Young's modulus (E_{LOC}) of 4 GPa was assumed. A local trabecular yield stress (σ_{yLOC}) of 66 MPa and elastic Poisson's ratio (ν_e) of 0.3 were also assumed (Harrison et al. 2008). Symmetric boundary conditions were imposed at the apparent level to simulate each loading configuration ensuring the specimen edges remained planar during loading and each model was loaded to 5 % apparent strain (v6.11 Abaqus Standard, Dassault Systémes Simulia Corp. Providence, RI).

In addition to μCT models, continuum models of the trabecular bone were also investigated in order to replicate the material behaviour (Kelly and McGarry 2012). Uniaxial, confined and hydrostatic compression loading were implemented to 5 % apparent strain, noting that the q–p ratio differs for each loading case (where q denotes the von Mises equivalent stress, and p is the pressure (hydrostatic) stress, see Appendix for details). The VM, crushable foam with isotropic hardening (CFI) and crushable foam with volumetric hardening (CFV) plasticity formulations are considered (v6.11 Abaqus Standard). All three plasticity formulations were calibrated in uniaxial compression to the μCT-based models, and the ability of each formulation to replicate the hydrostatic and confined compression behaviour of the μCT models was investigated. For the CFI and CFV plasticity formulations, the compression yield stress ratio (K), the ratio of the uniaxial to the hydrostatic yield stress, was determined from the μCT results. A plastic Poisson's ratio (ν_p) of 0.29 was assumed (Kelly and McGarry 2012). Parameter calibration was performed to identify an accurate solution for ν_e under hydrostatic compression.

2.2 Macroscale experimental testing and computational simulation of vertebral punch indentation

Mechanical testing of IFD subsidence was performed by indenting an 8 mm diameter punch into a lumbar ovine vertebral body, referred to as a full vertebral test (FVT). In order to visualise the trabecular deformation that occurs during the mechanical testing, testing was also performed on ovine vertebral bodies dissected in the sagittal plane and indented using a half-punch, referred to as a vertebral visualisation test (VVT). Eight L6 ovine vertebrae obtained from the PRTLI 'Bone for Life' project were frozen at −20 °C and thawed at 4 °C in phosphate buffer solution (PBS) for 24 h prior to mechanical testing. The transverse processes were removed at approximately 5 mm from where they joined the vertebral body using a bandsaw under constant irrigation (Jubilee VBS 360, Addison Saws Ltd., West Midlands, UK). The superior intervertebral discs were dissected using a scalpel and care was taken not to damage the vertebral endplate.

For the FVTs ($n = 5$), each vertebra was secured in a custom-made rig ensuring the superior endplate remained parallel to the test direction (Fig. 2). The inferior endplate was potted to a depth of approximately 19 mm in a rig using a low-melting point alloy. An 8 mm diameter slot drill was used to remove approximately 1 mm of the cortical bone from the central portion of the superior endplate until a complete surface of underlying trabecular bone was

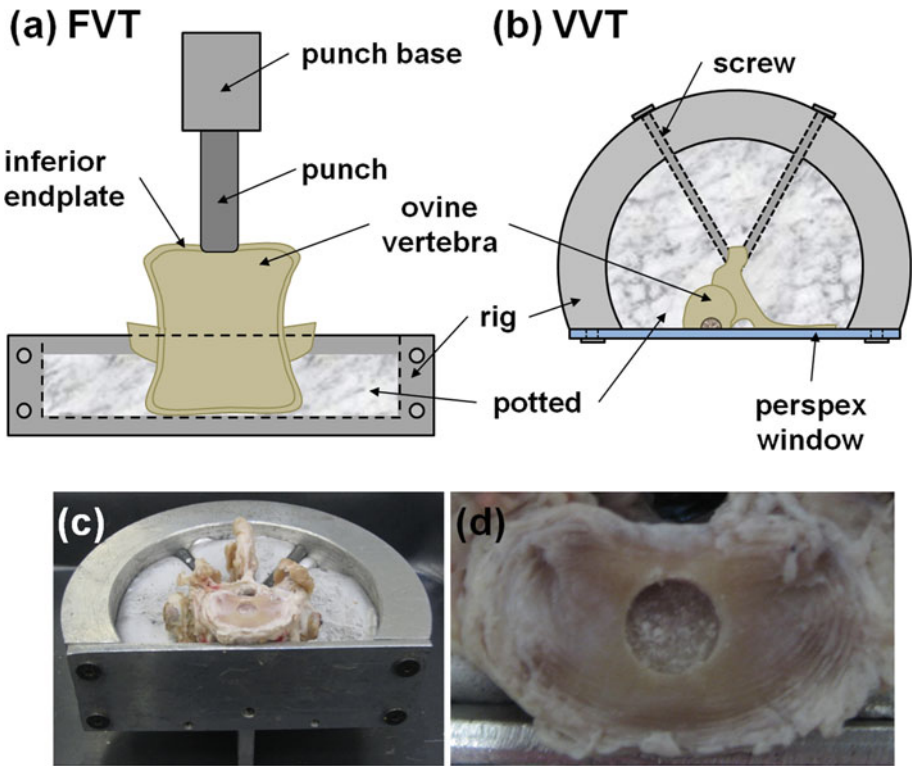

Fig. 2 Experimental testing **a** front view schematic of a full vertebral test (FVT) specimen potted in the testing rig, **b** plan view schematic of a vertebral visualisation test (VVT) specimen potted in the testing rig, **c** FVT specimen potted in the testing rig, **d** FVT specimen with drilled hole in the central vertebral endplate exposing the trabecular bone

observed. The potted specimens were mounted in a testing machine with a 30 kN load cell (model 4467, Instron Corp., Canton, MA, USA). To approximate an IFD, an 8 mm diameter solid cylindrical aluminium punch was used to apply an axial compressive load to the specimens at a rate of 5 mm/min to an indentation depth of 10 mm. One FVT specimen experienced significant modulus reduction during testing and was excluded, leaving four specimens for analysis.

For the VVTs ($n = 5$) (Fig. 2b), the vertebral bodies were cut in the sagittal plane using a bandsaw. An 8 mm diameter slot drill was used to create a semi-circular hole with a radius of 4 mm and a depth of approximately 1 mm at the centre of the endplate. A small brush and water hose were used to remove the excess marrow at the cut surface to expose the external trabecular bone struts. The vertebral cut surface was placed against a perspex window in a custom-made rig, creating a symmetry boundary condition, and was potted (~19 mm) in the rig and mounted on the Instron (Fig. 2b). The specimens were loaded in axial compression using a semi-circular punch (radius = 4 mm) also at a rate of 5 mm/min and to an indentation depth of 10 mm. In tandem with the mechanical tests, 2D video imaging of each VVT was performed using a camera. The experimental whitening regions were measured from selected frames at 4–8 mm indentation. Force-indentation curves were plotted for each specimen. The maximum force was defined as the maximum load following the linear portion of the force-indentation curve.

A macroscale continuum 2D axisymmetric FE model of an ovine lumbar vertebra was created consisting of approximately 375,000 linear triangular and quadrilateral elements (v6.11 Abaqus Explicit). The metallic punch was modelled as a rigid body as it is several orders of magnitude stiffer than the trabecular bone. The cortical bone was assumed to be homogenous, isotropic and linear elastic with an apparent Young's modulus (E_{APP}) of 22 GPa and an ν_e of 0.3 (Reilly and Burstein 1974). The trabecular bone was assumed to be homogenous and was modelled using five different plasticity formulations: VM; DP; CFI; CFV; and Hill. Following initial yield, perfectly-plastic behaviour (no strain hardening) was assumed for all formulations. Material parameter calibration was performed for the trabecular bone E_{APP} and apparent yield stress (σ_{yAPP}) to determine an accurate numerical solution for the experimental results. The ν_e was based on the microstructural results. For the DP plasticity formulation, a friction angle (β) of 2°, a flow stress ratio (K_{DP}), the ratio of the yield stress in triaxial tension to the yield stress in triaxial compression, of 1 and a dilation angle (ψ) of 0° were assumed. For the crushable foam plasticity formulations, the value of K was based on the microstructural results. A ν_p of 0.29 for the CFI plasticity formulation was assumed (Kelly and McGarry 2012). For the anisotropic Hill plasticity formulation, the yield stress ratios in the two transverse directions

were based on testing of the μCT models in the two transverse loading directions. Details of the five plasticity formulations are provided in the Appendix. Loads and boundary conditions were applied to replicate the experimental set-up. A frictionless surface-to-surface penalty contact algorithm was implemented between the punch and bone. An adaptive remeshing rule was used due to the large deformations that occur during loading.

3 Results

3.1 Computational results of a representative trabecular bone sample

The computed apparent stress–strain curves of the μCT-based trabecular bone models under uniaxial, hydrostatic and confined compression for a VM plasticity formulation are shown in Fig. 3a–c (black lines). The stress results in Fig. 3 are normalised, whereby the apparent stress (σ) is divided by the σ_{yAPP}. For the μCT model under uniaxial compression, a distinct apparent yield point is followed by a stress plateau (Fig. 3a). A ratio of the E_{APP} to the σ_{yAPP} of 79 is computed under uniaxial compression. The E_{APP} and σ_{yAPP} results are in agreement with previously reported experimental uniaxial compression results on ovine lumbar trabecular bone (Harrison et al. 2008). For confined compression, a very similar apparent stress–strain curve is computed for the μCT model, with a slightly higher σ_{yAPP} (Fig. 3c). The computed uniaxial and confined compression apparent stress–strain curves are similar to previous experimental results (Kelly and McGarry 2012). Under hydrostatic compression, similar yield behaviour is also computed for the μCT models with slight strain hardening evident post-yield (Fig. 3b). For the μCT models with a DP plasticity formulation assumed for the trabecular material, incorporating a friction angle ($\beta = 4°$; $K_{DP} = 1$; $\psi = 0°$) and strength asymmetry ($\beta = 0°$; $K_{DP} = 0.8$; $\psi = 0°$), similar yield points in the apparent stress–strain curve are predicted for hydrostatic and confined compression (results not presented) to that predicted for a VM plasticity formulation.

At an apparent strain of 2 %, trabecular yielding is evident in all three compression loading configurations, whereas at 5 % strain, near perfectly-plastic behaviour with little strain hardening is computed for the μCT models with a VM plasticity formulation for the trabecular material (Fig. 3). In Figs. 4 and 5, the local behaviour of individual trabeculae is shown at an apparent strain of 2 and 5 % for the μCT models under all three compression loading configurations. The computed contour plot results of equivalent plastic strain, von Mises equivalent stress (q) and pressure stress (p) are detailed. For all three loading configurations, the applied apparent strains result in non-uniform localised yielding of the trabeculae (Figs. 4a–c, 5a–c), which are more pronounced under hydrostatic compression. At both 2 and 5 % strain, greater local magnitudes and distributions of equivalent plastic strain, von Mises equivalent stress and pressure are predicted for hydrostatic compression (Figs. 4b, e, h, 5b, e, h). It is critical to note that, although the apparent boundary conditions are hydrostatic compression and the material behaviour of individual trabeculae are the simplistic

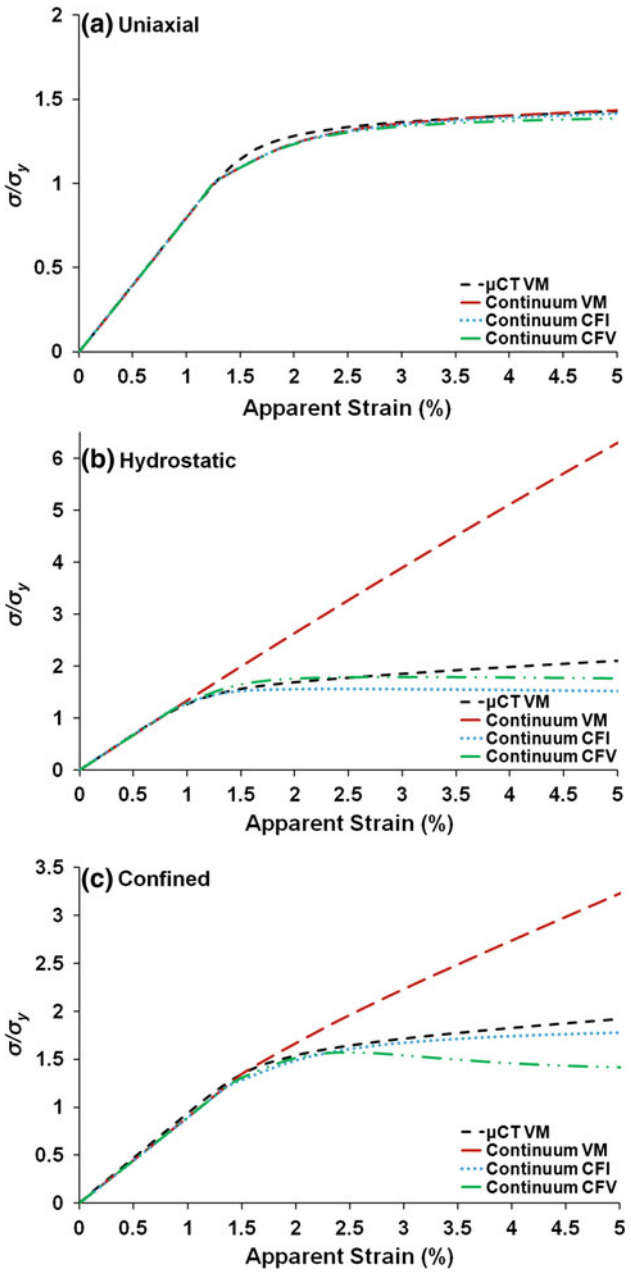

Fig. 3 Computational results of the μCT-based models and continuum-based models for the von Mises (VM), crushable foam with isotropic hardening (CFI) and crushable foam with volumetric hardening (CFV) plasticity formulations under **a** uniaxial compression, **b** hydrostatic compression, and **c** confined compression

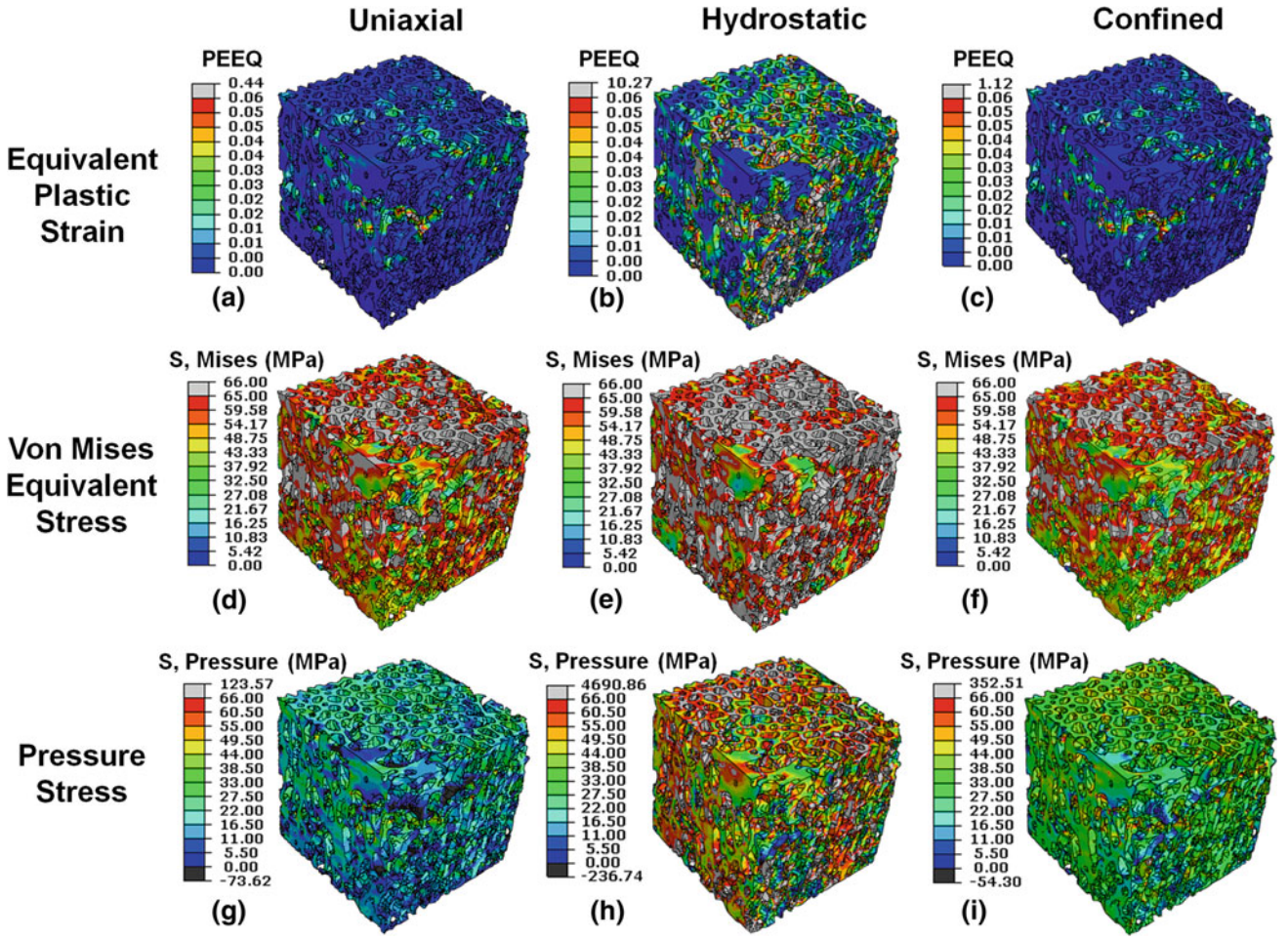

Fig. 4 Computational local equivalent plastic strain, von Mises equivalent stress, and pressure stress results at an apparent strain of 2 % for the μCT-based models for uniaxial, hydrostatic and confined compression using a von Mises plasticity formulation

pressure-independent VM plasticity formulation, extensive localised plastic yielding and plasticity occur due to the complex trabecular architecture (Figs. 4b, 5b). At 2 and 5 % strain, the plastic strain regions (Figs. 4a–c, 5a–c) correspond to comparable regions of high von Mises equivalent stress (Figs. 4d–f, 5d–f). It is clear from the μCT results that despite implementing a simplistic VM plasticity formulation for the trabecular material, the complex microarchitecture of the trabeculae causes a distinct yield point in the apparent stress–strain curve under all three compression loading configurations.

The ability of a continuum model of the trabecular bone with a VM plasticity formulation to replicate the μCT-based apparent level stress–strain curves is also considered in Fig. 3 (red lines). Under uniaxial compression, the continuum VM plasticity formulation is calibrated to the μCT results, where a distinctive yield point is followed by a stress plateau (Fig. 3a). Under hydrostatic compression, a ν_e of 0.21 is computed, which replicates the initial elastic behaviour very well (Fig. 3b). The continuum VM plasticity formulation cannot replicate the μCT results under hydrostatic compression and no yield is computed (by definition). A continuum-based VM plasticity formulation cannot achieve apparent yield under hydrostatic loading; therefore, a plasticity formulation that incorporates pressure-dependent yielding is necessary for a continuum-based representation of trabecular bone. Under confined compression, slight plastic deformation occurs for the continuum VM plasticity formulation and a poor match to the μCT results is achieved (Fig. 3c). For the continuum VM plasticity formulation, the apparent stresses at 5 % apparent strain are over predicted by a factor of 6.3 and 3.2 under hydrostatic and confined compression, respectively, when compared to the μCT results. A continuum model with a DP plasticity formulation does not have the ability to capture the yield behaviour of the μCT models under hydrostatic or confined compression due to its linear yield surface in the q–p plane and would produce similar over predicted results under hydrostatic compression to the continuum VM plasticity formulation.

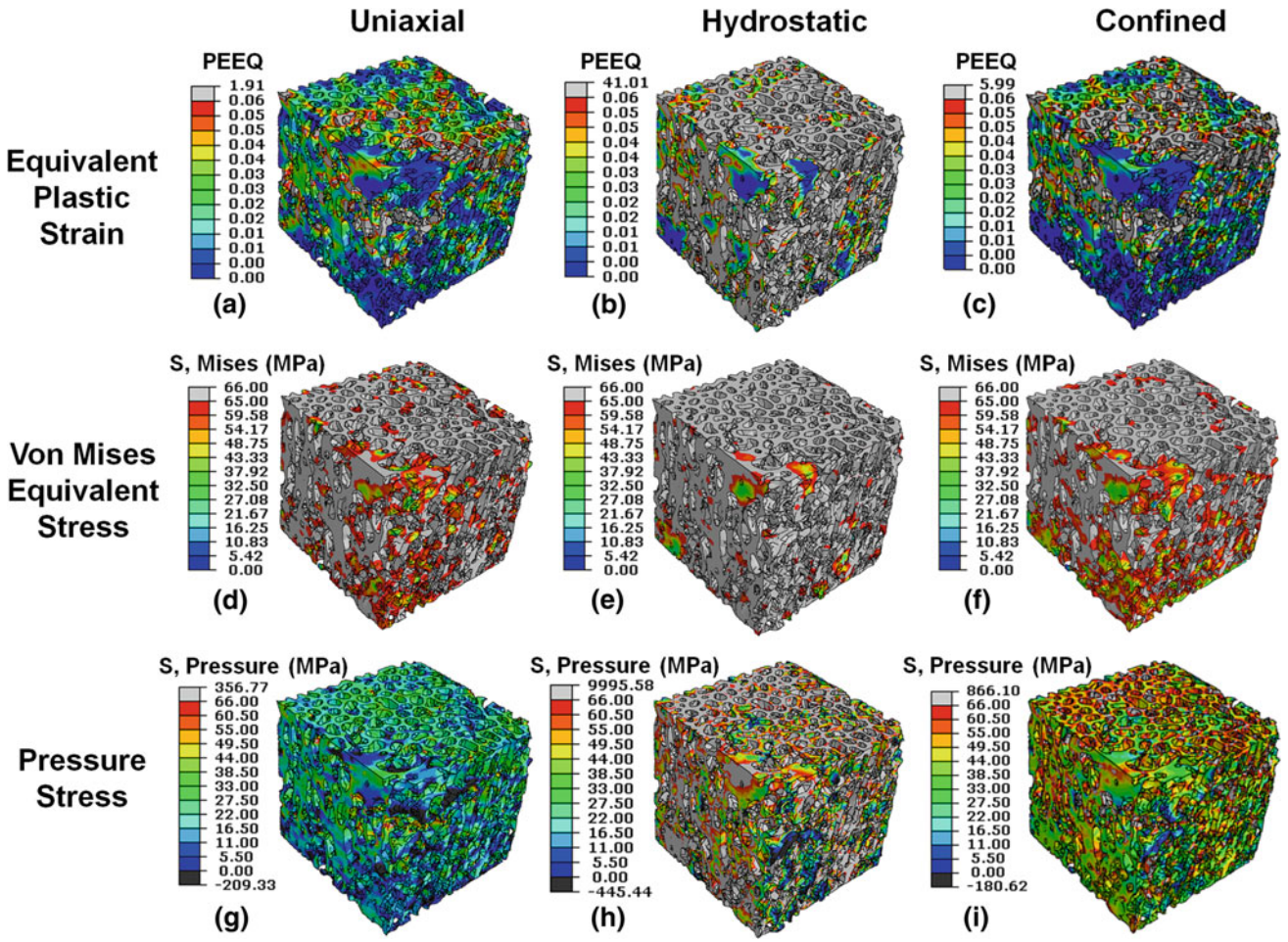

Fig. 5 Computational local equivalent plastic strain, von Mises equivalent stress, and pressure stress results at an apparent strain of 5 % for the μCT-based models for uniaxial, hydrostatic and confined compression using a von Mises plasticity formulation

Additionally, the ability of a continuum model with the CFI and CFV plasticity formulations to capture the μCT-based apparent level stress–strain curves is considered in Fig. 3 (blue and green lines). The CFI and CFV plasticity formulations were calibrated under uniaxial compression to the μCT results (Fig. 3a). For the crushable foam plasticity formulations, K was computed as 0.85 based on the μCT results. In contrast to the continuum VM plasticity formulation, a distinctive yield point is predicted for the CFI and CFV plasticity formulations under hydrostatic compression, approximating the μCT results very well (Fig. 3b). Although the stresses for the CFI and CFV plasticity formulations are slightly under predicted at higher strains for hydrostatic loading, they provide superior matches to the μCT results than the continuum VM plasticity formulation. As a validation, confined compression was performed and the CFI and CFV plasticity formulations predict the microstructural yield stress and post-yield behaviour quite well (Fig. 3c). The CFI plasticity formulation provides a better correlation with the μCT results under confined compression than the CFV plasticity formulation. For the CFV plasticity formulation, a hydrostatic yield stress ratio (K_t) of 0.5 (i.e., the ratio of the yield stress in hydrostatic tension to the initial yield stress in hydrostatic compression) provides a reasonable match to the μCT results under all three loading configurations. The continuum CFI and CFV plasticity formulations, which permit pressure-dependent yielding, replicate the μCT-based apparent stress–strain curves very well under all three loading configurations.

The μCT models reveal that when a pressure-independent VM plasticity formulation is assumed, the apparent yield behaviour of the trabecular bone is pressure dependent due to local yielding of trabeculae. The development of stress concentrations lead to localised yielding of trabeculae due to the microarchitecture. The VM plasticity formulation can predict apparent trabecular yielding under hydrostatic and confined compression loading only if the trabecular microstructure is considered concurrently. However, for a continuum representation of trabecular bone under hydrostatic or confined compression, it is essential to implement a

constitutive formulation, such as a crushable foam plasticity formulation, that has the ability to capture the pressure-dependent yield behaviour of the trabecular bone. Unlike VM and DP plasticity, for an increase in pressure, the crushable foam plasticity formulations lead to a lower von Mises equivalent stress at yield due to the elliptical yield surface in the q–p plane.

3.2 Macroscale experimental testing and computational simulation of vertebral punch indentation results

The experimental force-indentation curves for the macroscale indentation of a punch into vertebral trabecular bone specimens are shown in Fig. 6. The FVT and VVT results are shown in Fig. 6a, b where distinctive yielding is followed by a stress plateau. As only half-vertebrae are tested, the mean VVT force results in Fig. 6c are multiplied a factor of two, therefore comparing directly with the mean FVT results. Similar mean experimental results are measured for the FVTs and VVTs (scaled results) where yielding occurs at approximately 3 and 2.5 kN, respectively. Experimental (mean ± SD) maximum force results of 3.1 ± 0.7 and 1.5 ± 0.1 kN (scaled 3.0 ± 0.1 kN) are measured for the FVTs and VVTs.

The results of a VVT at indentation depths of 0, 2, 4, 6, 8 and 10 mm are shown in Fig. 7 where localised regions of trabecular bone whitening are observed directly below the punch. Whitening of trabecular bone has been shown to be evidence of localised plastic deformation, crushing and microdamage of trabeculae (Thurner et al. 2006, 2007; Jungmann et al. 2011) and is clearly evident below the punch at indentation depths of 2–10 mm. At 2 mm indentation, a whitened trabecular region is evident immediately below the punch, extending 3.2 ± 0.9 mm from the punch–bone interface (Fig. 7b). With increased indentation from 4 to 8 mm, the whitened trabecular region that advances below the punch does not increase substantially, extending 3.2 ± 0.4, 3.3 ± 0.6 and 3.4 ± 0.7 mm below the interface, respectively (Fig. 7c–e).

The macroscale computational predictions for punch indentation depths of 2–10 mm are shown in Fig. 8. The trabecular bone was modelled as a continuum and the material behaviour was modelled using the VM, DP, Hill, CFI and CFV plasticity formulations. The experimental FVT results (mean ± SD) are also shown in Fig. 8 for comparison. For the trabecular bone, an E_{APP} of 170 MPa and a ν_e of 0.21 replicate the initial pre-yield portion of the experimental results very well. With a trabecular bone σ_{yAPP} of 50 MPa, the VM plasticity formulation accurately predicts the initial yield behaviour; however, it cannot capture the experimental force plateau post-yield. Very similar results are also computed for the DP plasticity formulation ($\sigma_{yAPP} = 50$ MPa; $\beta = 2°$; $K_{DP} = 1$; $\psi = 0°$). At an indentation of over 3 mm, the forces for the VM and DP plasticity formulations exceed the experimental standard deviations, overestimating the force required to achieve punch indentation by 73 and 65 %, respectively. The anisotropic Hill plasticity formulation, with yield stress ratios in the transverse directions of 0.52 and 0.57 of the axial σ_{yAPP}, captures the initial yield behaviour very well. However, an over predicted force plateau is computed from 4 to 10 mm indentation that is outside the experimental standard deviations. The experimental yield and force plateau behaviour

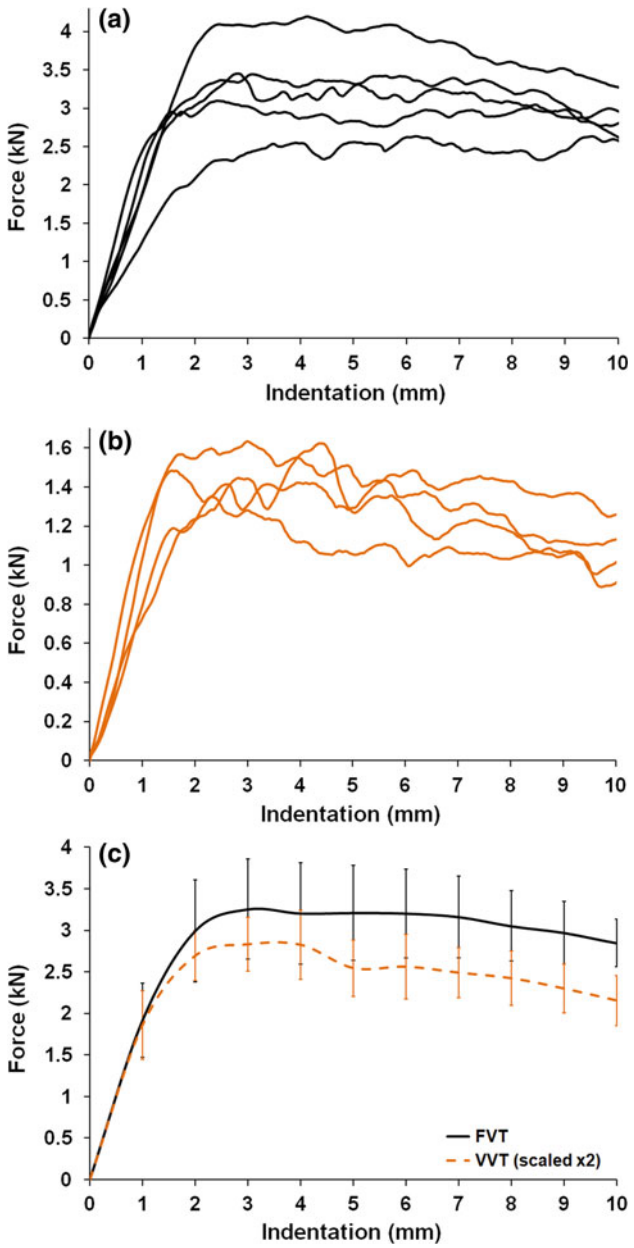

Fig. 6 **a** Experimental full vertebral test (FVT) results, **b** experimental vertebral visualisation test (VVT) results, **c** experimental results (mean ± SD) of the VVTs and FVTs. For purposes of comparison with FVT results, the VVT force results are scaled by a factor of two as only half of each vertebral specimen was tested

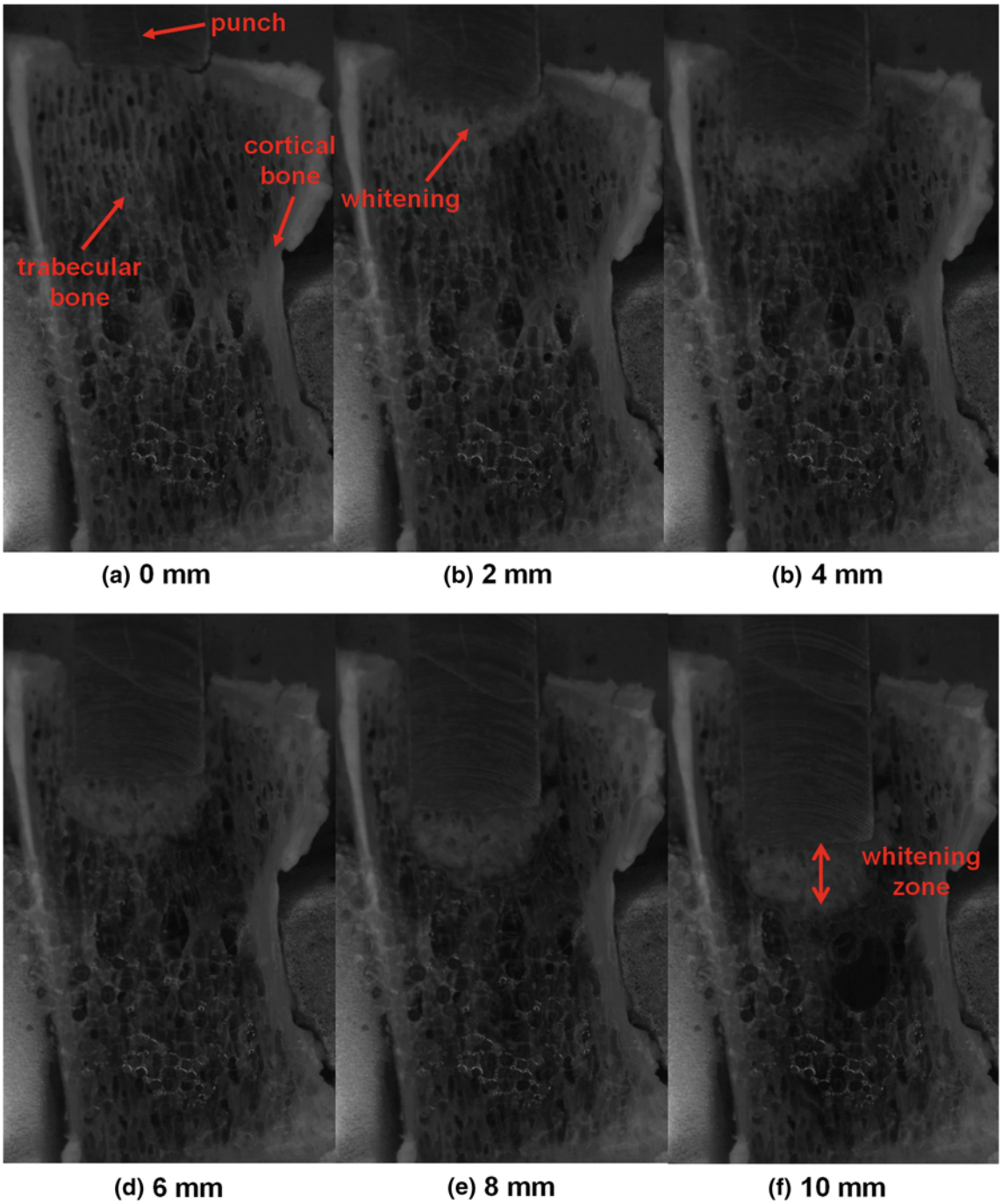

Fig. 7 Experimental images of a vertebral visualisation test (VVT) specimen captured at indentation depths of: **a** 0 mm **b** 2 mm; **c** 4 mm; **d** 6 mm; **e** 8 mm; and **f** 10 mm. A localised zone of trabecular bone whitening, indicating plastic deformation and damage, can be observed directly under the punch during subsidence

are captured very well by the CFI plasticity formulation ($\sigma_{\mathrm{yAPP}} = 50\,\mathrm{MPa}$; $K = 0.85$; $\nu_p = 0.29$), which are within the experimental standard deviations. For a CFV plasticity formulation ($\sigma_{\mathrm{yAPP}} = 50\,\mathrm{MPa}$; $K = 0.85$; $K_t = 0.5$), the initial yield and force plateau are slightly under predicted, but computed force values are within the standard deviations of the experimental results. When compared to the mean experimental FVT results, maximum errors in the force predictions of 32, 8 and 17 % occur for the Hill, CFI and CFV plasticity formulations, respectively.

Computational contour plot results of the equivalent plastic strain, von Mises equivalent stress and pressure of the

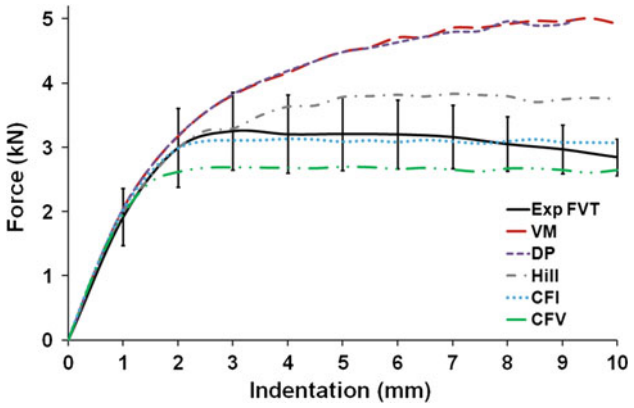

Fig. 8 Macroscale experimental and computational results of the full vertebra with 10 mm punch indentation for five different plasticity formulations: von Mises (VM); Drucker–Prager (DP); Hill; crushable foam with isotropic hardening (CFI); crushable foam with volumetric hardening (CFV)

punch indentation into the vertebral trabecular bone are depicted in Figs. 9, 10 and 11, respectively, for the VM, Hill, CFI and CFV plasticity formulations. Due to the similarity with the VM plasticity formulation results, contour plot predictions for the DP plasticity formulation are not presented. At a punch indentation depth of 2 mm, similar stress and strain results are evident for the VM, Hill, CFI and CFV plasticity formulations (Figs. 9a, 10a, 11a). In addition to the qualitative results in Figs. 9, 10 and 11, quantitative results are presented in Fig. 12 where the depths the plastic zone regions extend below the punch–bone interface are shown for all five plasticity formulations at 4, 6 and 8 mm punch indentation. In Fig. 12, the plastic regions are also compared to the experimentally (mean ± SD) observed whitening regions at the same indentation depths. As shown in Figs. 9 and 12, greater regions of equivalent plastic strain are computed for the VM and Hill plasticity formulations at 4–10 mm indentation than for the CFI and CFV plasticity formulations where the strains are much more localised. For VM plasticity, a non-yielding region (black in contour plot) is evident directly below the punch–bone interface at 4–10 mm indentation (Fig. 9b–e). In contrast, localised plastic yielding is evident directly below the interface for the CFI plasticity formulation in Fig. 9b–e which extends 3.1, 3.2, 3.1 and 3.1 mm from the interface at 4–10 mm indentation, respectively (Fig. 12). Whitening of the trabecular bone at the region immediately below the punch–bone interface is also observed experimentally (Fig. 7), with very similar regions and depths of whitening and plastic strain observed experimentally and for the CFI plasticity formulation (Fig. 12). Similar plastic strain depths are also predicted for the CFV plasticity formulation (Fig. 9b–e, 12); however, non-yielding regions are evident, which are not observed experimentally. An over predicted zone of plastic yielding is evident for the VM plasticity formulation (Fig. 9b–e) that enlarges below the punch with increased indentation, extending 5.1–6.3 mm from the interface at 4–10 mm indentation (Fig. 12). The Hill plasticity formulation over predicts the region of plastic yielding, which a maximum depth of 5.9 mm at 8 mm indentation (Figs. 9, 12). A larger plastic yielding region lateral to the punch is also predicted for the Hill plasticity formulation (Fig. 9). Experimental images reveal that such whitening is not evident lateral to the punch (Fig. 7).

At 4–10 mm indentation in Fig. 10b–e, distinct localised regions of high von Mises equivalent stress (shown in red and grey) are evident for the CFI and CFV plasticity formulations in contrast to the VM and Hill plasticity formulations where a much greater area of increased stress is computed. Although the peak von Mises equivalent stress is similar for all of the plasticity formulations, the regions of high stress increase in depth with increased punch indentation for the VM in comparison with CFI and CFV plasticity formulations where the regions remain nearly constant. In contrast to the von Mises equivalent stress results in Fig. 10, the magnitudes of the peak compressive pressure (+ve) in Fig. 11 are much greater for the VM and Hill plasticity formulations than for the CFI and CFV plasticity formulations. At 4–10 mm indentation, peak compressive pressures of 74–126 MPa and 99–101 MPa occur for VM and Hill plasticity, respectively, in comparison with 52–55 MPa and 54–59 MPa for the CFI and CFV plasticity formulations, respectively (Fig. 11b–e). At 4–10 mm indentation (Fig. 11b–e), localised high pressures (>50 MPa, shown in grey) are evident for CFI and CFV plasticity extending 0.5–0.7 mm and 0.2–1.0 mm from the punch–bone interface, respectively. In contrast to the crushable foam plasticity formulation results, high interface pressures in the VM and Hill plasticity formulations are more pronounced extending 1.8–3.5 mm and 3.2–3.7 mm, respectively, below the punch at 4–10 mm indentation (Fig. 11b–e). Interestingly, for VM plasticity, the high interface pressures (Fig. 11b–e) contrast with the plastic strain results where a non-yielding region is predicted immediately below the punch (Fig. 9b–e).

The VM plasticity formulation results in large over predicted distributions of both pressure and von Mises equivalent stress (Figs. 10, 11) and the resulting indentation forces are hence over predicted (Fig. 8). Similarly, over predicted distributions of pressure and von Mises equivalent stress are evident for the Hill plasticity formulation (Figs. 10, 11) and the indentation forces are not within the experimental standard deviations (Fig. 8). In contrast to the VM and Hill results, plasticity in the CFI and CFV plasticity formulations are concentrated at the interface (Fig. 9) due to the fact an increase in pressure leads to a lower von Mises equivalent stress at yield for crushable foam plasticity. For the CFI plasticity formulation, the high interface pressures correspond to a comparable area of plasticity (Fig. 11).

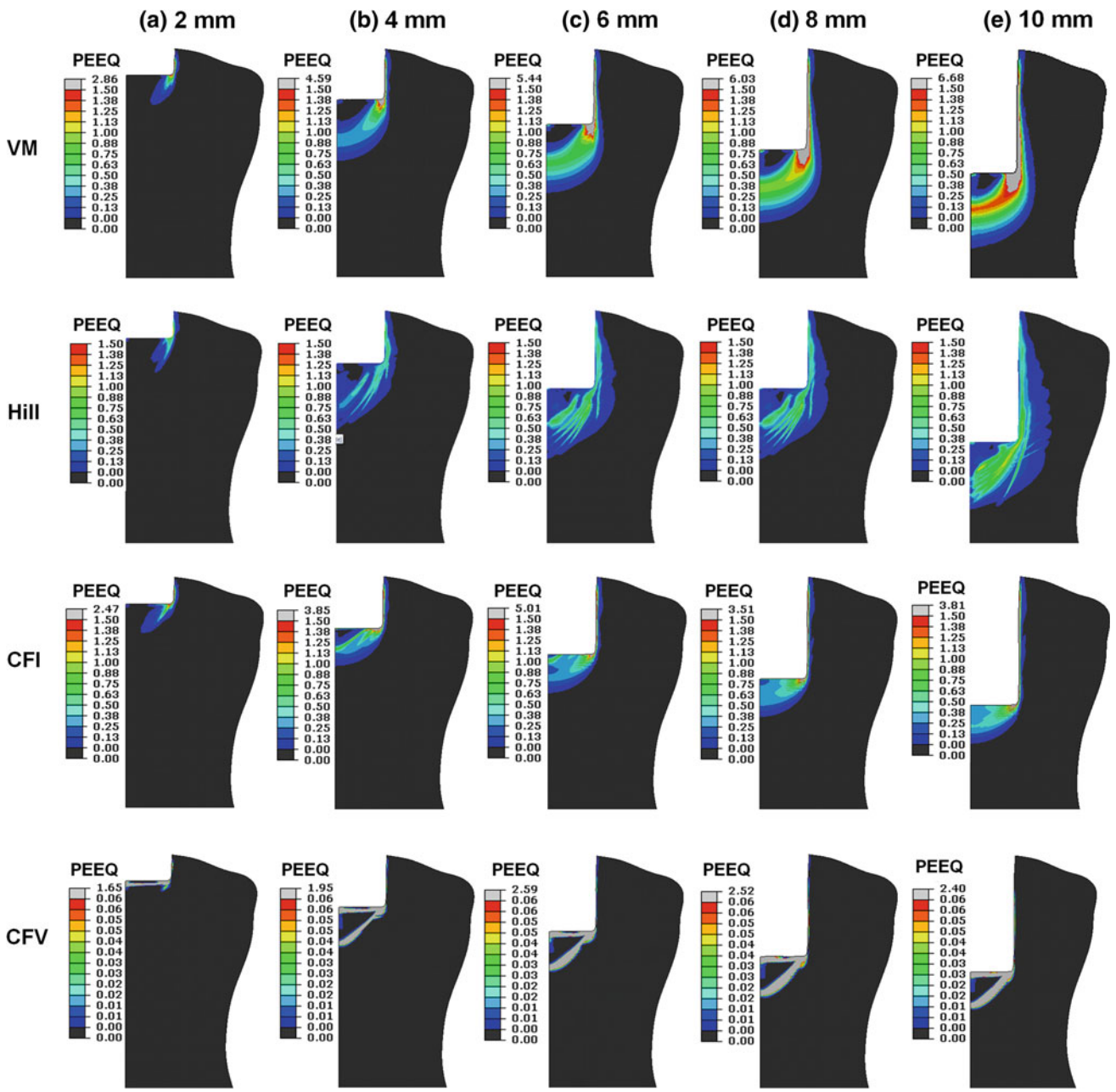

Fig. 9 Computational equivalent plastic strain contour plots of the macroscale vertebral models at a indentation depth of 2, 4, 6, 8 and 10 mm for trabecular bone with the von Mises (VM), Hill and crushable foam (CFI, CFV) plasticity formulations. The cortical bone and punch are removed for clarity

4 Discussion

The microstructural FE simulations of trabecular bone reveal a distinctive yield point at the apparent level under uniaxial, hydrostatic and confined compression. Simulations reveal that under hydrostatic compression, localised stress concentrations occur at a microscale (trabeculae level), resulting in a distinctive yield point in the apparent stress–strain curve. This distinctive response at the apparent level can be accurately captured by a continuum model using a pressure-dependent CFI or CFV plasticity formulation. At the macroscale, the vertebral subsidence experiments quantify localised regions of whitened trabecular bone directly under the punch, which remain approximately constant in size with increased indentation. Macroscale vertebral IFD subsidence simulations further emphasise the importance

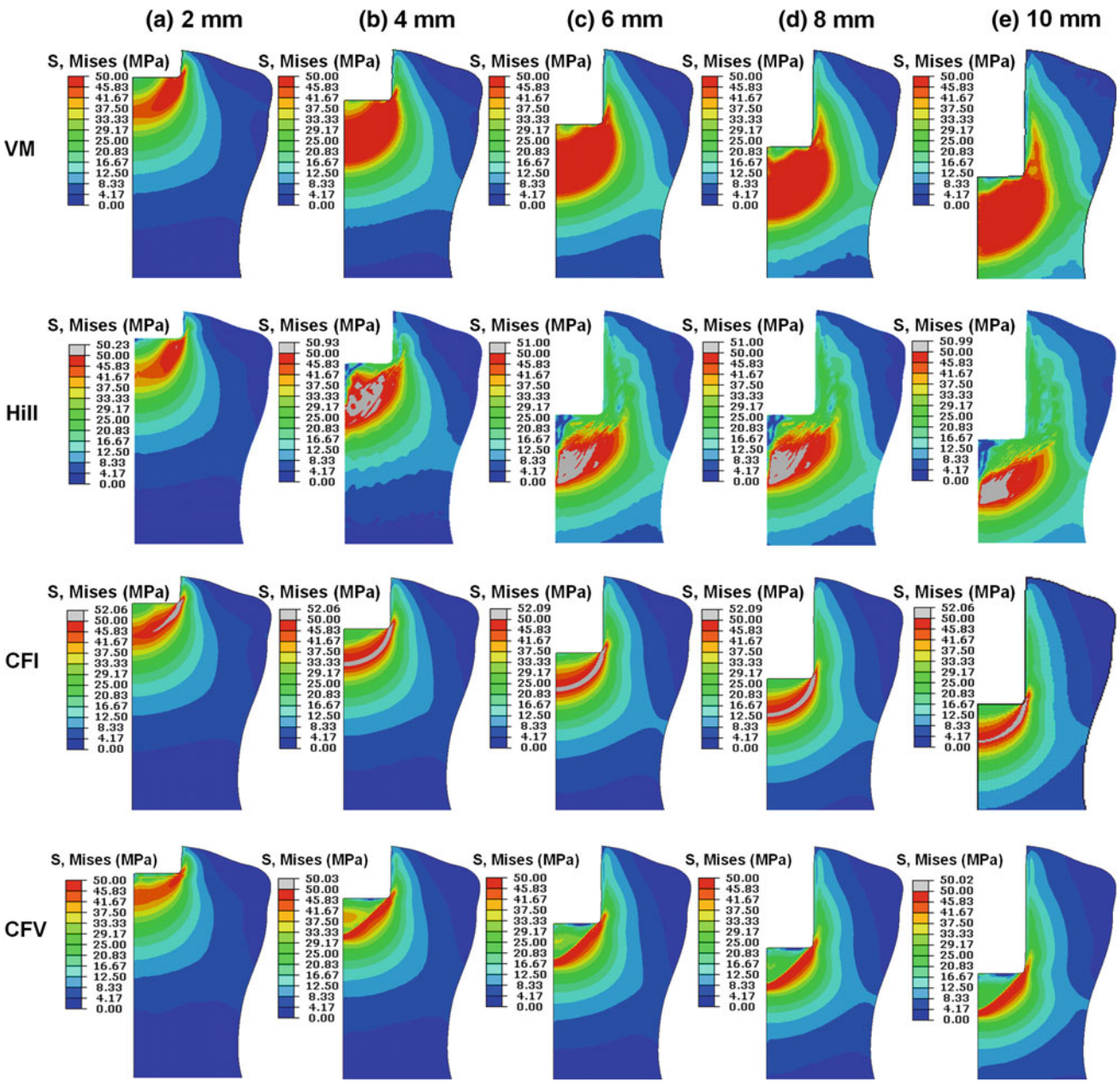

Fig. 10 Computational von Mises equivalent stress contour plots of the macroscale vertebral models at a indentation depth of 2, 4, 6, 8 and 10 mm for trabecular bone with the von Mises (VM), Hill and crushable foam (CFI, CFV) plasticity formulations. The cortical bone and punch are removed for clarity

of implementing an appropriate pressure-dependent plasticity formulation (with an elliptical yield surface in the $q-p$ plane) in macroscale continuum models of trabecular bone. The CFI plasticity formulation provides accurate predictions of subsidence force in addition to computation of a highly localised region of plastic deformation of trabecular bone directly under the punch, correlating strongly with experimentally observed whitening zones.

In the microstructural models, the trabecular material is modelled using a simple pressure-independent VM plasticity formulation; hence, yielding in the trabecular microstructure occurs due to concentrations of the von Mises equivalent stress and not due to localised hydrostatic stress in the trabecular material. However, when apparent hydrostatic compression is applied to a μCT model, a distinctive yield point is observed in the apparent stress–strain curve, similar to the multiaxial compression results of Rincon-Kohli and Zysset (2009). This clearly demonstrates that the apparent pressure-dependent yielding of trabecular bone, observed by Kelly and McGarry (2012), can occur as a result of localised

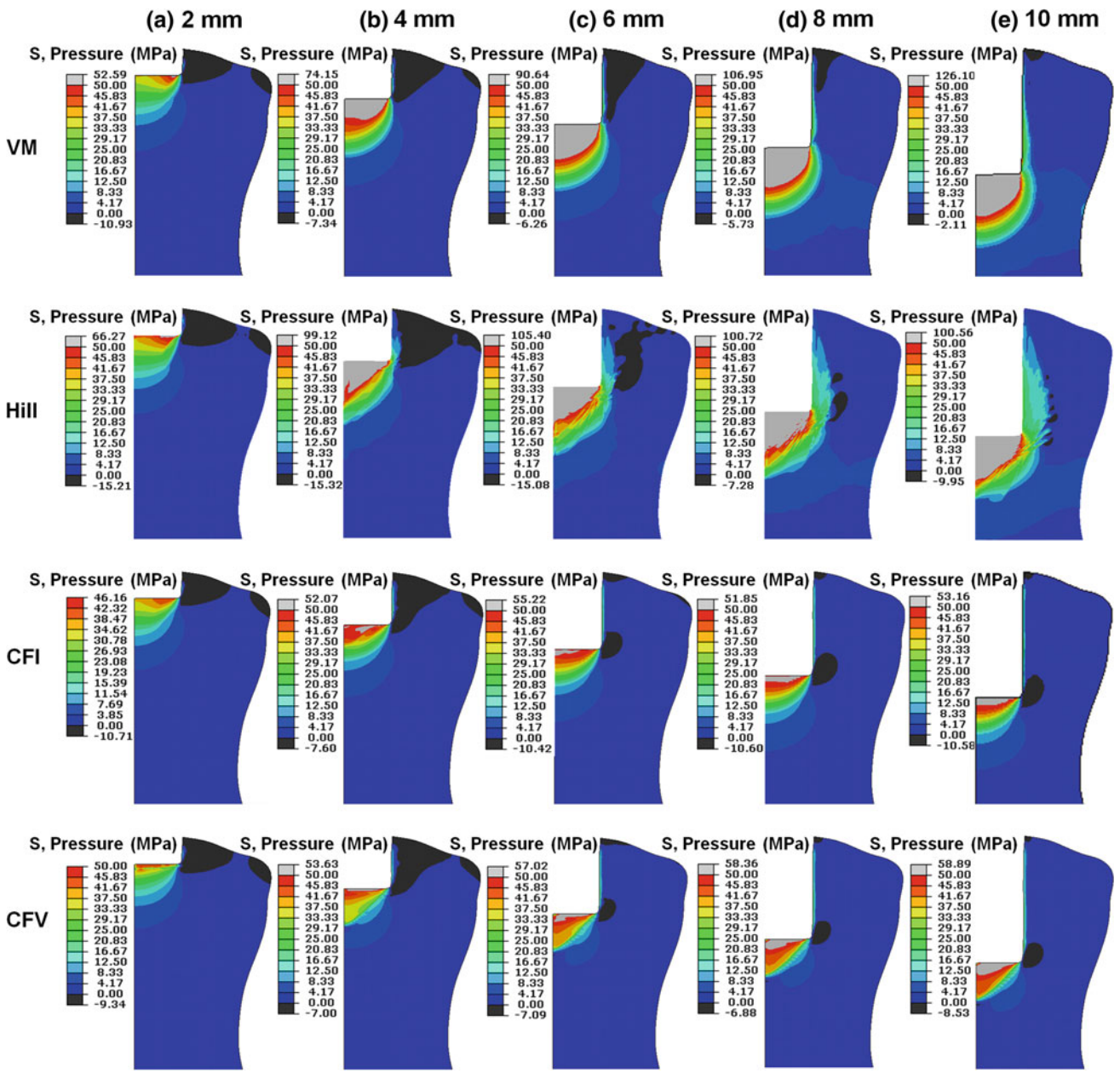

Fig. 11 Computational pressure stress contour plots of the macroscale vertebral models at a indentation depth of 2, 4, 6, 8 and 10 mm for trabecular bone with the von Mises (VM), Hill and crushable foam (CFI, CFV) plasticity formulations. The cortical bone and punch are removed for clarity

stress concentrations and yielding in the trabeculae at a microstructural level without the requirement that the localised yield is pressure dependent. This distinctive yield and plateau behaviour are also observed under hydrostatic compression for a μCT model with a DP plasticity formulation. This demonstrates that the link between localised microstructural yielding and the macroscopic behaviour of trabecular bone is not dependent on the specific plasticity formulation implemented at the microstructural level. Its is also demonstrated that to capture reported differences in tensile and compressive yield stress using a μCT model, a plasticity formulation that incorporates this strength asymmetry must be used at a material level. It is revealed that the inclusion of the trabecular microarchitecture in the μCT models is a more dominant factor in predicting apparent yield behaviour than the specific form of the plasticity formulation used to represent the material behaviour of the trabecular microstructure. For example, a μCT model with a simplistic VM plasticity formulation at the trabecular material level is sufficient to elucidate the experimentally observed apparent level pressure-dependent yielding of trabecular bone. As experimental validation of pure hydrostatic compression is not

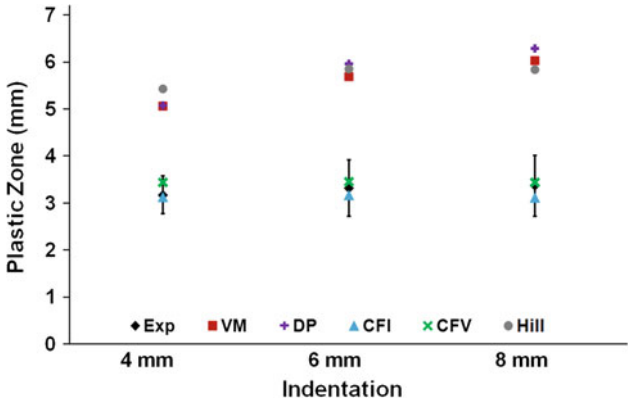

Fig. 12 Mean (±SD) of plastic regions extending from the punch–bone interface in the experimental VVTs and macroscale computational models at 4, 6 and 8 mm trabecular indentation with the von Mises (VM), Drucker–Prager (DP) ($\beta = 2°$; $K_{DP} = 1$; $\psi = 0°$), Hill, crushable foam with isotropic hardening (CFI) ($K = 0.85$; $\nu_p = 0.29$) and crushable foam with volumetric hardening (CFV) ($K = 0.85$; $K_t = 0.5$) plasticity formulations

available, confined compression simulations are also performed using the microstructural geometry. Predicted apparent stress–strain curves under confined compression exhibit a distinctive yield point followed by a stress plateau, similar to the experimental results of Kelly and McGarry (2012) and Charlebois et al. (2010b).

Previous microstructural voxel-based FE models have focused on the simulation of uniaxial compression of trabecular bone using linear elastic material models (Harrison et al. 2008; Nagaraja et al. 2005; Mc Donnell et al. 2010; Van Rietbergen et al. 1995; Müller and Rüegsegger 1995). The non-linear behaviour of microstructural trabecular bone models has also been modelled by reducing the elastic modulus of the trabecular material to 5 % when critical principal strain is computed at a material point (Bayraktar et al. 2004; Bayraktar and Keaveny 2004; Niebur et al. 2000, 2002; Guillén et al. 2011; Verhulp et al. 2008; Harrison et al. 2012). Niebur et al. (2000) based such criteria on macroscopic testing of cortical bone by Reilly and Burstein (1975). Under uniaxial compression, (Harrison et al. 2012) incorporated material damage using the principal strain-based criterion and fracture through element removal and cohesive forces in the trabecular microarchitecture. Also based on the testing of cortical bone specimens, Verhulp et al. (2008) implemented the principal strain-based criterion in addition to a perfectly-plastic VM plasticity formulation for the uniaxial compression testing of trabecular bone. Van Rietbergen et al. (1995) and Boyd et al. (2002) considered confined compression loading that was limited to the linear elastic regime, hence offering no insight into multiaxial yield behaviour. Using the principal strain-based criterion at a trabecular level, biaxial compression strain and normal-shear strain of μCT-based trabecular specimens have been simulated (Bayraktar et al. 2004; Niebur et al. 2002). Niebur et al. (2002) proposed a multiple-surface yield criterion with two intersecting yield ellipses for the on-axis and transverse yield points, whereas Bayraktar et al. (2004) proposed a modified super-ellipsoid yield criterion. The present study provides predictions of the apparent yield behaviour of microstructural models of trabecular bone under confined and hydrostatic compression. As trabecular bone is naturally constrained by the surrounding cortex, multiaxial loading configurations such as hydrostatic and confined compression are particularly relevant and should be carefully characterised in order to provide accurate predictions of in vivo trabecular bone behaviour.

Complex multiaxial loading of trabecular bone is encountered during bone fracture, screw pullout and press-fit device implantation (Cawley et al. 2012) in addition to vertebral IFD subsidence as demonstrated in the present study. Despite this, a relatively small number of experimental studies have performed confined or multiaxial compression testing of trabecular bone specimens. Linde and Hvid (1989) performed confined compression solely in the elastic regime, whereas Kelly and McGarry (2012) and Charlebois et al. (2010b) performed confined compression post-yield to large inelastic strains. The triaxial compression (Rincon-Kohli and Zysset 2009; Keaveny et al. 1999) and axial-shear strength (Fenech and Keaveny 1999) of trabecular bone have also been investigated. The current study highlights the need for extensive further multiaxial experimental testing and corresponding microstructural computational simulations to further elucidate the inelastic behaviour of trabecular bone under complex loading configurations.

Microstructural based trabecular bone geometries have been applied to macroscale applications of trabecular bone. Microstructural voxel-based geometries of vertebrae have been investigated assigning identical linear elastic material properties to the cortex and trabeculae (Eswaran et al. 2006; Harrison and McHugh 2010). Significant limitations are associated with such an approach given the high computational expense. Using idealised microstructural trabecular geometry (lattice beam elements) inside simplified vertebral geometry, McDonald et al. (2010) implemented a VM plasticity formulation for the trabecular microstructure. The present study demonstrates that simulation of multiaxial loading of representative samples of trabecular bone microstructure can inform the development of more accurate continuum models that can then be used for macroscale applications with finite deformation, accurate contact conditions and complex non-linear material behaviour.

The μCT models in the present study elucidate that localised stress concentrations and yielding in the trabecular microstructure affect the apparent level pressure-dependent plasticity of trabecular bone observed experimentally by Kelly and McGarry (2012). A continuum representation of trabecular bone using the CFI or CFV plasticity formula-

tions replicates the apparent stress–strain curve predicted by the μCT models. Under confined compression, the crushable foam plasticity formulations accurately capture the apparent yield point and post-yield behaviour of trabecular bone predicted by the μCT models and observed experimentally by Kelly and McGarry (2012). The crushable foam plasticity formulations capture the apparent pressure-dependent yield observed under hydrostatic compression in the μCT models. In the triaxial compression loading of Rincon-Kohli and Zysset (2009), an increase in radial compressive stress results in a decrease in the axial stress required to cause yield. A piecewise yield surface was experimentally uncovered by Rincon-Kohli and Zysset (2009) in which the compressive quadrant is qualitatively similar to the crushable foam plasticity formulation. The predicted compression yield stress ratio, K, of 0.85 for the crushable foam plasticity formulations in the present study for ovine trabecular bone is comparable to the previously reported value of 1 for bovine tibial trabecular bone (Kelly and McGarry 2012).

As expected, a continuum VM plasticity formulation cannot capture the pressure-dependent yield behaviour of trabecular bone under hydrostatic or confined compression. Despite this, continuum pressure-independent plasticity formulations have been widely used for trabecular bone including the VM (Keyak 2001; Keyak and Falkinstein 2003) and strain-based plasticity formulations (Gupta et al. 2007; Cowin and He 2005). The present study has shown that a continuum-based pressure-dependent DP plasticity formulation is also inadequate in capturing the inelastic trabecular behaviour although previously implemented for trabecular bone (Bessho et al. 2007; Derikx et al. 2011). Kelly and McGarry (2012) and the present study have demonstrated that continuum-based plasticity formulations such as the DP and Mohr-Coulomb formulations that have linear yield surfaces in the $q-p$ plane are inappropriate for modelling trabecular bone, although they have been shown to capture the inelastic behaviour of cortical bone (Feerick and McGarry 2012; Mullins et al. 2009). Plasticity formulations such as the modified super-ellipsoid yield criterion (Bayraktar et al. 2004), the Tsai-Wu plasticity formulation (Fenech and Keaveny 1999; Keaveny et al. 1999) and a cellular solid criterion (Fenech and Keaveny 1999) have also been proposed to describe the multiaxial yielding of trabecular bone. The Tsai-Wu plasticity formulation has been shown to reasonably predict the combined axial-shear strength (Fenech and Keaveny 1999) and to poorly predict the triaxial compressive stress (Keaveny et al. 1999) of trabecular bone. Representing trabecular bone morphology, Zysset and co-workers employed inelastic continuum material models where fabric tensors and volume fraction describe the heterogeneity and anisotropy of the bone, respectively (Charlebois et al. 2010a,b; Rincon-Kohli and Zysset 2009; Chevalier et al. 2008; Zysset and Rincon-Kohli 2006; Zysset and Curnier 1996). Although such fabric-based models have the advantage of incorporating trabecular inhomogeneity and anisotropy, they require microstructural properties of the trabeculae derived from methods such as μCT data.

In the present study, the video imaging of the macroscale VVTs reveals regions of localised trabecular whitening immediately adjacent to the punch, which remain almost constant with increased indentation. Such whitening regions signify localised plastic deformation, crushing and microdamage of trabeculae (Thurner et al. 2006, 2007; Jungmann et al. 2011). The experimental yield type force-indentation curves are captured very well using the CFI plasticity formulation. Additionally, the CFI plasticity formulation predicts localised trabecular bone yield regions immediately below the punch that correlate closely with the experimentally measured whitening regions. The force-indentation curves and plastic zone size are also reasonably captured by a CFV plasticity formulation that incorporates asymmetric behaviour in hydrostatic tension and compression. However, non-yielding regions are predicted for the CFV plasticity formulation that are not observed experimentally. The VM, DP and Hill plasticity formulations over predict the experimental forces required to resist subsidence. In comparison with the experimental measurements, the VM, DP and Hill plasticity formulations also predict excessively large plastic zones that further enlarge with increased indentation. The Hill plasticity formulation, an extension of the VM plasticity formulation that incorporates anisotropic yield behaviour, cannot replicate the experimental results. The DP plasticity formulation cannot predict the correct subsidence force or plastic zone size due to its linear yield surface in the q–p plane that results in an increased yield stress with increased pressure. The VM plasticity formulation also predicts non-yielding regions at the punch–bone interface, which do not correlate with the experimentally observed whitening regions. The experimental study of Warden and Davy (2010), investigating trabecular damage after mechanical testing of IFDs to 1 and 2.5 % strain, reports localised histologic damage and permanent deformation close to the implant–bone interface. The localised plastic zone reported by Warden and Davy (2010) supports our macroscale experimental results and CFI plasticity formulation predictions. The present study highlights the importance of implementing a pressure-dependent plasticity formulation with an elliptical yield surface in the q–p plane, such as the crushable foam plasticity formulations, when investigating continuum macroscale inelastic behaviour of trabecular bone, leading to accurate prediction of subsidence force and plastic zone size. As revealed in the present study, the VM, DP and Hill plasticity formulations will over predict the subsidence force and the plastic zone size.

The current study has some limitations that should be addressed in future work. In the macroscale experimental testing, only one indenter geometry was investigated. Further experimental studies with various endplate preparation

techniques, IFD geometries and strain rates would be advantageous to further investigate the mechanics of vertebral subsidence. It is possible that the stress concentrations induced due to IFD implantation may result in remodelling of the underlying bone, which could alter the mechanics of subsidence. A 2D axisymmetric model was used for the macroscale computational analysis. A fully 3D geometry proved to be excessively computationally demanding due to the large inelastic deformation requiring the use of a remeshing algorithm. The predicted anisotropic behaviour of the μCT trabecular models was incorporated into the macroscale indentation simulations using a continuum-based Hill plasticity formulation. Unlike the CFI and CFV plasticity formulations, a continuum-based Hill plasticity formulation is limited in replicating the experimentally observed trabecular behaviour as it does not incorporate pressure-dependent yielding. While the current study demonstrates the advantages of using a crushable foam plasticity formulation over the VM, DP and Hill plasticity formulations for predicting macroscale vertebral subsidence force and plastic zone size, the authors suggest that ongoing work should entail the simulation of subsidence using alternative plasticity formulations proposed for trabecular bone such as the fabric-based models of Zysset and co-workers, the modified super-ellipsoid yield criterion (Bayraktar et al. 2004), the Tsai-Wu plasticity formulation (Fenech and Keaveny 1999; Keaveny et al. 1999) or a plasticity formulation that incorporates pressure-dependent yield, anisotropic yield and strength asymmetry. The incorporation of such a plasticity formulation that includes damage and fracture may also lead to enhanced results and may be a focus of a future study.

The present study provides a significant advance in the simulation of macroscale vertebral IFD subsidence. To the authors knowledge, the current study is the first to investigate the pressure-dependent inelastic deformation of trabecular bone during vertebral device subsidence. Additionally, the study provides a correlation between trabecular whitening and regions of plastic deformation during vertebral device subsidence. The plastic zone regions predicted using the CFI plasticity formulation correlate well with the experimental whitening regions, which remain approximately constant in size with increased subsidence. Previous continuum-based macroscale studies provide extremely limited predictions of subsidence as they have relied on linear elastic material models (Polikeit et al. 2003a,b; Lim et al. 2001). The present study demonstrates the importance of representing pressure-dependent plasticity in continuum models of trabecular bone in order to accurately simulate the vertebral subsidence.

Experimental studies on subsidence have predominantly focused on endplate preparation and implant geometry with the maximum failure load being measured to evaluate the subsidence resistance (Lim et al. 2001; Oxland et al. 2003; Steffen et al. 2000; Lowe et al. 2004; Hollowell et al. 1996; Closkey et al. 1993). Oxland et al. (2003) found a significant decrease in failure load and stiffness for endplate removal. Lowe et al. (2004) found that mean failure loads for complete removal were significantly lower than partially removed or intact endplates. Using full and peripheral support devices, Steffen et al. (2000) found no difference in failure loads with intact endplates and removed (device sitting on periphery) endplates. Lim et al. (2001) found a reduction in compressive strength with complete endplate removal. According to Hollowell et al. (1996), the endplate thickness may not be sufficient to resist subsidence. The current study provides significant insight into trabecular bone plasticity and demonstrates that the pressure-dependent crushable foam plasticity formulations provide accurate macroscale continuum simulation of vertebral IFD subsidence. In particular, the current study demonstrates that the crushable foam plasticity formulations provide a reasonable representation of the multiaxial behaviour predicted by a μCT model of the trabecular microstructure, while also providing a close correlation with macroscale experimentation. It is, therefore, suggested that the crushable foam plasticity formulations could be used to accurately model the inelastic behaviour of trabecular bone for macroscale applications in which an explicit representation of the microstructure is not computationally feasible. Such accurate macroscale continuum models could be used to improve the design of IFDs and help guide clinical issues such as endplate preparation and device selection.

5 Conclusions

In summary, the μCT models elucidate that localised stress concentrations and yielding in the trabecular microstructure affect the apparent level pressure-dependent plasticity of trabecular bone. It is demonstrated that simulation of multiaxial loading of representative samples of the trabecular bone microstructure can inform the development of accurate continuum models that can then be used for macroscale applications. The crushable foam plasticity formulations provide a reasonable link between the microscale and macroscale behaviour of trabecular bone. The multiaxial behaviour of a representative sample of trabecular bone microstructure is accurately replicated by crushable foam plasticity formulations. When applied to a macroscale study of vertebral device subsidence, the crushable foam plasticity formulations provide an accurate prediction of the experimental behaviour. Experimental trabecular whitening during vertebral device subsidence is quantified, and it is demonstrated that it is critically important to use a continuum plasticity formulation that replicates the inelastic pressure-dependent behaviour of trabecular bone in order to accurately simulate the experimental behaviour. Unlike the VM, DP and Hill plasticity formulations, continuum-based CFI and CFV plasticity

formulations capture the macroscale inelastic pressure-dependent yield behaviour of trabecular bone leading to the accurate prediction of subsidence force and plastic zone size during vertebral device subsidence. In conclusion, the study provides insight into the role of the trabecular microarchitecture in the macroscale multiaxial behaviour of trabecular bone. Furthermore, correct simulation of the pressure-dependent yield behaviour of trabecular bone in a continuum model of vertebral subsidence is shown to provide strong agreement with experimental observations.

Acknowledgments The authors would like to thank Mr. Patrick Kelly B.Eng from the Mechanical Engineering Laboratory National University of Ireland Galway for technical assistance and David Nolan for insightful discussion. The authors wish to acknowledge the SFI/HEA Irish Centre for High-End Computing (ICHEC) for the provision of computational facilities and support; the College of Engineering and Informatics, National University of Ireland Galway for providing a postgraduate scholarship for Nicola Kelly.

Appendix

Von Mises constitutive plasticity formulation

Yield criterion: $F = q$

where the von Mises equivalent stress is given as $q = \sqrt{\frac{3}{2}S{:}S}$, and the deviatoric stress tensor S is obtained from the stress tensor σ such that $S = \sigma + pI$ noting that the pressure stress is given as $p = -\frac{1}{3}trace(\sigma)$.

Drucker–Prager constitutive plasticity formulation

$$\begin{aligned} &\text{Yield criterion :} \quad F = t - p\text{Tan}(\beta) - d = 0 \\ &\qquad\qquad\quad t = \frac{q}{2}\left[1 + \frac{1}{K_{\text{DP}}} - \left(1 - \frac{1}{K_{\text{DP}}}\right)\left(\frac{r}{q}\right)^3\right] \\ &\text{Flow potential :} \quad G = t - p\tan\psi \end{aligned}$$

where t is the Drucker–Prager deviatoric stress measure, β is the friction angle of the material, d is the material cohesion, K_{DP} is flow stress ratio, r is the third invariant of deviatoric stress, and ψ is the dilation angle (Drucker and Prager 1951).

Hill constitutive plasticity formulation

Yield Criterion:

$$F = \sqrt{L(\sigma_y-\sigma_z)^2+M(\sigma_z-\sigma_x)^2+N(\sigma_x-\sigma_y)^2+2T\tau_{yz}^2+2U\tau_{zx}^2+2V\tau_{xy}^2}$$

$$L = \frac{\sigma_0^2}{2}\left(\frac{1}{\bar{\sigma}_y^2}+\frac{1}{\bar{\sigma}_z^2}-\frac{1}{\bar{\sigma}_x^2}\right) \quad M = \frac{\sigma_0^2}{2}\left(\frac{1}{\bar{\sigma}_z^2}+\frac{1}{\bar{\sigma}_x^2}-\frac{1}{\bar{\sigma}_y^2}\right)$$

$$N = \frac{\sigma_0^2}{2}\left(\frac{1}{\bar{\sigma}_x^2}+\frac{1}{\bar{\sigma}_y^2}-\frac{1}{\bar{\sigma}_z^2}\right) \quad T = \frac{3}{2}\left(\frac{\tau_0}{\bar{\tau}_{yz}}\right) \quad U = \frac{3}{2}\left(\frac{\tau_0}{\bar{\tau}_{xz}}\right)$$

$$V = \frac{3}{2}\left(\frac{\tau_0}{\bar{\tau}_{xy}}\right)$$

where L, M, N, T, U and V are material constants, σ_i are the direct stress components in the principal directions of anisotropy, τ_{ij} are the shear stress components, $\bar{\sigma}_i$ are the uniaxial yield stresses in the principal directions of anisotropy, and $\bar{\tau}_{ij}$ are the shear yield stresses with respect to the axis of anisotropy (Hill 1948).

Crushable foam with isotropic hardening constitutive plasticity formulation

Yield criterion: $F = \sqrt{q^2 + \alpha^2 p^2} - B = 0$

$$B = \alpha p_c \quad \alpha = \frac{3K}{\sqrt{9-K^2}} \quad K = \frac{\sigma_c^0}{p_c^0}$$

Flow potential: $G = \sqrt{q^2 + \beta^2 p^2}$ $\quad \beta = \frac{3}{\sqrt{2}}\sqrt{\frac{1-2\upsilon_p}{1+\upsilon_p}}$

where α is the shape of the yield ellipse in the $q-p$ plane, B is the size of the yield ellipse, p_c is the yield stress in hydrostatic compression, K is the compression yield stress ratio, σ_c^0 is the initial yield stress in uniaxial compression, p_c^0 is the initial yield stress in hydrostatic compression, β is the ellipse for the potential flow, and υ_p is the plastic poisson's ratio (Deshpande and Fleck 2000).

Crushable foam with volumetric hardening constitutive plasticity formulation

Yield criterion: $F = \sqrt{q^2 + \alpha^2(p - p_0)^2} - B = 0$

$$\alpha = \frac{3K}{\sqrt{(3K_t + K)(3 - K)}} \quad K = \frac{\sigma_c^0}{p_c^0} \quad K_t = \frac{p_t}{p_c^0}$$

Flow potential: $G = \sqrt{q^2 + \frac{9}{2}p^2}$

where p_0 is the centre of the yield ellipse, K_t is the hydrostatic yield stress ratio, and p_t is the yield stress in hydrostatic tension.

References

Bayraktar HH, Keaveny TM (2004) Mechanisms of uniformity of yield strains for trabecular bone. J Biomech 37(11):1671–1678

Bayraktar HH, Gupta A, Kwon RY, Papadopoulos P, Keaveny TM (2004) The modified super-ellipsoid yield criterion for human trabecular bone. J Biomech Eng 126(6):677–684

Bessho M, Ohnishi I, Matsuyama J, Matsumoto T, Imai K, Nakamura K (2007) Prediction of strength and strain of the proximal femur by a CT-based finite element method. J Biomech 40(8):1745–1753

Beutler WJ, Peppelman WC (2003) Anterior lumbar fusion with paired BAK standard and paired BAK proximity cages: subsidence incidence, subsidence factors, and clinical outcome. Spine J 3(4): 289–293

Boyd SK, Müller R, Zernicke RF (2002) Mechanical and architectural bone adaptation in early stage experimental osteoarthritis. J Bone Miner Res 17(4):687–694

Cawley DT, Kelly N, Simpkin A, Shannon FJ, McGarry JP (2012) Full and surface tibial cementation in total knee arthroplasty: a biomechanical investigation of stress distribution and remodeling in the tibia. Clin Biomech 27(4):390–397

Charlebois M, Jirasek M, Zysset PK (2010a) A nonlocal constitutive model for trabecular bone softening in compression. Biomech Model Mechanobiol 9(5):597–611

Charlebois M, Pretterklieber M, Zysset PK (2010b) The role of fabric in the large strain compressive behavior of human trabecular bone. J Biomech Eng 132:1–10

Chen L, Yang H, Tang T (2005) Cage migration in spondylolisthesis treated with posterior lumbar interbody fusion using BAK cages. Spine 30(19):2171–2175

Chevalier Y, Charlebois M, Pahr D, Varga P, Heini P, Schneider E, Zysset P (2008) A patient-specific finite element methodology to predict damage accumulation in vertebral bodies under axial compression, sagittal flexion and combined loads. Comput Method Biomech 11(5): 477–487. doi:10.1080/10255840802078022

Choi JY, Sung KH (2006) Subsidence after anterior lumbar interbody fusion using paired stand-alone rectangular cages. Eur Spine J 15(1):16–22

Closkey RF, Parsons JR, Lee CK, Blacksin MF, Zimmerman MC (1993) Mechanics of interbody spinal fusion. Analysis of critical bone graft area. Spine 18(8):1011

Cowin SC, He QC (2005) Tensile and compressive stress yield criteria for cancellous bone. J Biomech 38(1):141–144

Derikx LC, Vis R, Meinders T, Verdonschot N, Tanck E (2011) Implementation of asymmetric yielding in case-specific finite element models improves the prediction of femoral fractures. Comput Method Biomech 14(02):183–193

Deshpande VS, Fleck NA (2000) Isotropic constitutive models for metallic foams. J Mech Phys Solids 48(6–7):1253–1283

Drucker DC, Prager W (1951) Soil mechanics and plastic analysis or limit design. Division of Applied Mathematics, Brown University, Brown University. Division of Applied, Mathematics United States. Office of Naval, Research

Eswaran SK, Gupta A, Adams MF, Keaveny TM (2006) Cortical and trabecular load sharing in the human vertebral body. J Bone Miner Res 21(2): 307–314. doi:10.1359/jbmr.2006.21.2.307

Feerick EM, McGarry JP (2012) Cortical bone failure mechanisms during screw pullout. J Biomech 45(9):1666–1672

Fenech CM, Keaveny TM (1999) A cellular solid criterion for predicting the axial-shear failure properties of bovine trabecular bone. J Biomech Eng 121(4):414–422

Goldstein SA (1987) The mechanical properties of trabecular bone: dependence on anatomic location and function. J Biomech 20 (11–12):1055–1061

Guillén T, Zhang QH, Tozzi G, Ohrndorf A, Christ HJ, Tong J (2011) Compressive behaviour of bovine cancellous bone and bone analogous materials, microCT characterisation and FE analysis. J Mech Behav Biomed Mater 4(7):1452–1461

Gupta A, Bayraktar H, Fox J, Keaveny T, Papadopoulos P (2007) Constitutive modeling and algorithmic implementation of a plasticity-like model for trabecular bone structures. Comput Mech 40(1): 61–72. doi:10.1007/s00466-006-0082-5

Harrison N, McHugh P (2010) Comparison of trabecular bone behavior in core and whole bone samples using high-resolution modeling of a vertebral body. Biomech Model Mechanobiol 9(4): 469–480. doi:10.1007/s10237-009-0188-8

Harrison NM, McDonnell PF, O'Mahoney DC, Kennedy OD, O'Brien FJ, McHugh PE (2008) Heterogeneous linear elastic trabecular bone modelling using micro-ct attenuation data and experimentally measured heterogeneous tissue properties. J Biomech 41(11):2589–2596

Harrison NM, McDonnell P, Mullins L, Wilson N, O'Mahoney D, McHugh PE (2012) Failure modelling of trabecular bone using a non-linear combined damage and fracture voxel finite element approach. Biomech Model Mechanobiol 1–17. doi:10.1007/s10237-012-0394-7

Hill R (1948) A theory of the yielding and plastic flow of anisotropic metals. Proc Roy Soc Lond 193(1033):281–297

Hollowell JP, Vollmer DG, Wilson CR, Pintar FA, Yoganandan N (1996) Biomechanical analysis of thoracolumbar interbody constructs: how important is the endplate. Spine 21(9): 1032–1036

Jungmann R, Szabo ME, Schitter G, Yue-Sing Tang R, Vashishth D, Hansma PK, Thurner PJ (2011) Local strain and damage mapping in single trabeculae during three-point bending tests. J Mech Behav Biomed Mater 4(4):523–534

Keaveny TM, Borchers RE, Gibson LJ, Hayes WC (1993) Trabecular bone modulus and strength can depend on specimen geometry. J Biomech 26(8):991–1000

Keaveny TM, Wachtel EF, Zadesky SP, Arramon YP (1999) Application of the Tsai-Wu quadratic multiaxial failure criterion to bovine trabecular bone. J Biomech Eng 121:99

Kelly N, McGarry JP (2012) Experimental and numerical characterisation of the elasto-plastic properties of bovine trabecular bone and a trabecular bone analogue. J Mech Behav Biomed Mater 9:184–197

Keyak JH (2001) Improved prediction of proximal femoral fracture load using nonlinear finite element models. Med Eng Phys 23(3):165–173

Keyak JH, Falkinstein Y (2003) Comparison of in situ and in vitro CT scan-based finite element model predictions of proximal femoral fracture load. Med Eng Phys 25(9):781–787

Keyak JH, Lee IY, Nath DS, Skinner HB (1996) Postfailure compressive behavior of tibial trabecular bone in three anatomic directions. J Biomed Mater Res 31(3):373–378

Kopperdahl DL, Keaveny TM (1998) Yield strain behavior of trabecular bone. J Biomech 31(7):601–608

Lim TH, Kwon H, Jeon CH, Kim JG, Sokolowski M, Natarajan R, An HS, Bj Andersson G (2001) Effect of endplate conditions and bone mineral density on the compressive strength of the graft-endplate interface in anterior cervical spine fusion. Spine 26(8): 951–956

Linde F, Hvid I (1989) The effect of constraint on the mechanical behaviour of trabecular bone specimens. J Biomech 22(5):485–490

Lowe TG, Hashim S, Wilson LA, O'Brien MF, Smith DAB, Diekmann MJ, Trommeter J (2004) A biomechanical study of regional endplate strength and cage morphology as it relates to structural interbody support. Spine 29(21):2389–2394

Mc Donnell P, Harrison N, McHugh PE (2010) Investigation of the failure behaviour of vertebral trabecular architectures under uni-axial compression and wedge action loading conditions. Med Eng Phys 32(6):569–576

McDonald K, Little J, Pearcy M, Adam C (2010) Development of a multi-scale finite element model of the osteoporotic lumbar vertebral body for the investigation of apparent level vertebra mechanics and micro-level trabecular mechanics. Med Eng Phys 32(6): 653–661

Morgan EF, Keaveny TM (2001) Dependence of yield strain of human trabecular bone on anatomic site. J Biomech 34(5):569–577

Müller R, Rüegsegger P (1995) Three-dimensional finite element modelling of non-invasively assessed trabecular bone structures. Med Eng Phys 17(2):126–133

Mullins LP, Bruzzi MS, McHugh PE (2009) Calibration of a constitutive model for the post-yield behaviour of cortical bone. J Mech Behav Biomed Mater 2(5):460–470

Nagaraja S, Couse TL, Guldberg RE (2005) Trabecular bone microdamage and microstructural stresses under uniaxial compression. J Biomech 38(4):707–716

Niebur GL, Feldstein MJ, Yuen JC, Chen TJ, Keaveny TM (2000) High-resolution finite element models with tissue strength asymmetry accurately predict failure of trabecular bone. J Biomech 33(12):1575–1583

Niebur GL, Feldstein MJ, Keaveny TM (2002) Biaxial failure behavior of bovine tibial trabecular bone. J Biomech Eng 124(6):699–705

Oxland TR, Grant JP, Dvorak MF, Fisher CG (2003) Effects of endplate removal on the structural properties of the lower lumbar vertebral bodies. Spine 28(8):771–777

Polikeit A, Ferguson SJ, Nolte LP, Orr TE (2003a) Factors influencing stresses in the lumbar spine after the insertion of intervertebral cages: finite element analysis. Eur Spine J 12(4):413–420

Polikeit A, Ferguson SJ, Nolte LP, Orr TE (2003b) The importance of the endplate for interbody cages in the lumbar spine. Eur Spine J 12(6):556–561. doi:10.1007/s00586-003-0556-5

Prendergast PJ, McHugh PE (2004) Topics in bio-mechanical engineering. In: Proceeding of the 1st symposium on biomechanical engineering, Ireland. Trinity Centre for Bio-Engineering, pp 58–93

Reilly DT, Burstein AH (1974) The mechanical properties of cortical bone. J Bone Jt Surg Am 56(5):1001–1022

Reilly DT, Burstein AH (1975) The elastic and ultimate properties of compact bone tissue. J Biomech 8(6):393–396, 397405

Rincon-Kohli L, Zysset P (2009) Multi-axial mechanical properties of human trabecular bone. Biomech Model Mechanobiol 8(3): 195–208. doi:10.1007/s10237-008-0128-z

Røhl L, Larsen E, Linde F, Odgaard A, Jørgensen J (1991) Tensile and compressive properties of cancellous bone. J Biomech 24(12):1143–1149

Steffen T, Tsantrizos A, Aebi M (2000) Effect of implant design and endplate preparation on the compressive strength of interbody fusion constructs. Spine 25(9):1077–1084

Thurner PJ, Erickson B, Schriock Z, Langan J, Scott J, Zhao M, Weaver JC, Fantner GE, Turner P, Kindt JH (2006) High-speed photography of the development of microdamage in trabecular bone during compression. J Mater Res 21(5):1093–1100

Thurner PJ, Erickson B, Jungmann R, Schriock Z, Weaver JC, Fantner GE, Schitter G, Morse DE, Hansma PK (2007) High-speed photography of compressed human trabecular bone correlates whitening to microscopic damage. Eng Fract Mech 74(12):1928–1941

Van Rietbergen B, Weinans H, Huiskes R, Odgaard A (1995) A new method to determine trabecular bone elastic properties and loading using micromechanical finite-element models. J Biomech 28(1):69–81

Verhulp E, Van Rietbergen B, Müller R, Huiskes R (2008) Micro-finite element simulation of trabecular-bone post-yield behaviour—effects of material model, element size and type. Comput Method Biomech 11(4): 389–395. doi:10.1080/10255840701848756

Warden KE, Davy DT (2010) Localized trabecular damage adjacent to interbody fusion devices. Spine 35(8):874–880

Zysset PK, Curnier A (1996) A 3D damage model for trabecular bone based on fabric tensors. J Biomech 29(12):1549–1558

Zysset P, Rincon-Kohli L (2006) An alternative fabric-based yield and failure criterion for trabecular bone. In: Holzapfel GA, Ogden RW (eds) Mechanics of biological tissue. Springer, Berlin, pp 457–470